Source study of the 24 August 2016 M_w=6.8 Chauk earthquake, Myanmar

Hasbi A Shiddiqi[1], Pa Pa Tun[2], Tun Lin Kyaw[2], and Lars Ottemöller[1]

[1]Department of Earth Science, University of Bergen, Allègaten 41, N-5007 Bergen, Norway.

[2]Department of Meteorology and Hydrology, Office No. 5, Ministry of Transport and Communications, Zeya Htani Road, Nay Pyi Taw, Myanmar.

Abstract

The source process of an intra-slab intermediate depth earthquake (h=90 km) that occurred near Chauk, Central Myanmar on 24 August 2016 was investigated using teleseismic body-wave inversion. The focal mechanism solution showed a thrust mechanism with nearly vertical or sub-horizontal fault planes. The slip inversion results for both fault planes gives similar variances and show a simple slip distribution. The fault-plane ambiguity was resolved by analyzing apparent source-time functions for teleseismic stations affected by directivity. Based on this analysis, we prefer the sub-horizontal fault plane where the rupture propagated down-dip. The T-axis showed down-dip extension while the P-axis showed slab normal compression. We obtained an effective fault length of 20 km and effective fault width of 18 km. A Stress drop of 20 bars was estimated by using the relation of effective fault dimension and seismic moment obtained from the slip inversion. Furthermore, we tested the stress drop, and the assumption of quality factor, which is adopted from the Mexican subduction zone, by conducting ground motion modeling at five regional strong motion stations. The stress drop of 20 bars can produce reasonable ground motion for these stations. One of the most prevailing hypothesis of the generating mechanism of sub-horizontal faulting in intermediate-depth is related to the dehydration embrittlement which either reactivated an existing fault before it was subducted or newly created fault after, e.g., due to slab unbending processes.

Introduction

An intermediate-depth earthquake with Mw(USGS)=6.8 struck near the Chauk township, Central Myanmar on 24 August 2016. The largest aftershock, magnitude Mb(USGS)=4.5, occurred within 23 minutes of the mainshock, overlapping with the coda of the mainshock. A total of nine smaller aftershocks were reported by the Department of Meteorology and Hydrology of Myanmar (DMH). However, most of these were recorded by three or fewer stations, which means the locations are not reliable. The mainshock was felt across Myanmar, Bangladesh, western Thailand, and northeast India. A damage survey was conducted following the earthquake and according to the report, the earthquake killed three persons (Zaw et al. 2017). The earthquake affected Old Bagan, a historic site 35 km northeast of the epicenter, where damage was observed at 180 historical pagodas. Previously, the Old Bagan site suffered damage from the Mw=6.9, 1975 earthquake.

A second reconnaissance survey was conducted two weeks after the earthquake by a group from the Myanmar Earthquake Committee, Department of Archaeology of Myanmar, and Mahidol University, Thailand (Zaw et al. 2017). This more detailed survey confirmed that there was some degree of damage to over 270 monuments, including ancient pagodas in Old Bagan, with 50 of them classified as heavily damaged. The monuments were constructed between the 9th and 13th centuries without proper earthquake resistance design. Even though these pagodas were repaired after the 1975 earthquake, similar damage patterns were observed in 2016. Light to moderate damages also occurred to modern buildings in the nearby regions.

Myanmar is situated in an active tectonic region resulting from the interaction between the Eurasian, Indian, Burma, and Sunda plates. Major crustal faults have caused devastating earthquakes in Myanmar, including the 2011 M_w=6.8 Tarlay earthquake in eastern Myanmar, which occurred on the Nam Ma fault and resulted in at least 74 deaths (Tun et al. 2014); and the 2012 M_w=6.8 Shwebo earthquake in central Myanmar, which occurred on the Sagaing fault

(Wang et al. 2014). While most damaging earthquakes in the Myanmar region occurred on shallow crustal faults, intra-slab earthquakes can still cause some damage, especially in areas with thick sediments (Kundu and Gahalaut 2012). Furthermore, it is known that quite extensive damage occurred after the 1975 Bagan earthquake, and there are several examples globally of damaging intermediate depth earthquakes, such as M_w(GCMT)=7.5 Vrancea 1977, M_w(GCMT)=7.6 Padang 2009, and M_w(GCMT)=7.1 Central Mexico 2017.

Although the most damaging earthquakes in Myanmar over past last 100 years were related to the Sagaing fault and other shallow faults, intermediate-depth earthquakes have also caused minor to moderate damage. Between 1900 and 2016, there were at least sixteen strong intermediate-depth earthquakes ($M \geq 6.5$) (depth between 70 and 200 km) according to the catalog from the International Seismological Centre (2015; http://www.isc.ac.uk). The most damaging earthquakes were the 1975 M_w=7 event (centroid depth 95.7 km, Global CMT Solution) and the 1988 M_w=7.2 event (centroid depth 100.5 km, Global CMT Solution). The 1975 event, which was located 56 km north of the 2016 event, caused quite extensive damage to pagodas and other historical structures in Old Bagan (Aung 2017). For the 1975 earthquake, an intensity of VIII was reported at several places close to the epicenter, i.e., at Myaing (32 km NE), Bagan (40 km SE), and Nyaung-U (38.5 km SE). The 1988 event, which is located ~470 km north of the 2016 event, was the largest intermediate depth event in the region since the last century and had a maximum intensity of VIII (Kayal 2010). It was felt throughout northeast India, Bangladesh and Myanmar, killed four people and caused damage to structures, roads, and railways (Kayal 2010).

Studying the source process of the Chauk 2016 earthquake can help us to understand the stress and deformation within the subducting Indian slab. There are several critical physical parameters that we investigated in this study, including source geometry and complexity, and stress drop. We studied the source process of the earthquake by inverting for moment tensor and a finite-slip model using teleseismic P- and SH-waves data. While the fault plane ambiguity cannot be resolved using body-wave inversion, we resolved it by investigating source-time function directivity observed at teleseismic stations. We estimated the static stress drop by using parameters we obtained from the slip inversion results, i.e., seismic moment and effective source dimension. Furthermore, we performed stochastic ground motion modeling and compared the results to data from four newly installed strong motion stations in Myanmar (Thiam et al. 2017) and one station in Thailand. This is the first time such a damaging earthquake was recorded following a major network upgrade in early 2016.

Intermediate depth seismicity in Myanmar

The Indo-Burman range (IBR) is located between the Himalayan belt in the north, and Sumatra-Andaman subduction in the south (Figure 1a). It extends across western Myanmar with a length of ~1400 km. The Indian plate moves north-northeast with a highly oblique motion at a velocity of 47 mm/year toward the Eurasian and Burma plates (Paul et al. 2001). Some parts of this oblique motion are accommodated by pure strike-slip faults (e.g., the Sagaing Fault), thrust faults along the IBR, and also by the subduction of the Indian plate in western Myanmar (Le Dain et al. 1984). Some part of this motion can be also accommodated by the shearing motion of the Indian plate beneath the Burma plate as suggested by several studies, e.g., (Le Dain et al. 1984; Kumar et al. 1996). Intermediate depth earthquakes, generally shallower than 200 km, occur along the IBR, apart from the southern section toward the Andaman Sea (Pesicek et al. 2010; Hurukawa et al. 2012) (Figure 1b). However, the subducted Indian plate, seen as high P-wave velocity anomaly, beneath the Burma plate continues down to ~500 km before flattening out toward the east (Li et al. 2008). Seismicity studies beneath the Myanmar region (Ni et al. 1989; Hurukawa et al. 2012) showed that the Wadati-Benioff zone is bent from north to south.

Whether the Indo-Burma subduction is still active or not is an on-going discussion. Several authors argued that the subduction is no longer active based on investigations of focal mechanisms and stress inversion studies along the IBR (e.g., Kumar et al. 1996; Purnachandra Rao and Kumar 1999). These studies found that the predominant P-axis directions are NNE-SSW, respectively, which are nearly parallel to the Indian plate motion. It is suggested that these patterns are due to the Indian slab dragging beneath the IBR due to nearly parallel Indian plate movement. Satyabala (1998), however, argued that subduction is still active, as reflected by the down-dip T-axis directions. These predominant T-axis directions can be caused by active slab pull force. A recent geodetic study revealed that the megathrust in the region accommodates 13-17 mm/year of plate convergence (Steckler et al. 2016).

Previous focal mechanism analyses showed that P-axis azimuths, especially in the northern region, are predominantly trench-parallel, which could be related to the highly oblique motion of the Indian plate to the NNE-SSW direction and T-axis azimuths are trench normal reflecting the down-dip extension (Ni et al. 1989; Kumar et al. 1996). Furthermore, stress inversion of focal mechanisms of intermediate depth seismicity indicated that the major principal stress (σ_1) has a north-south trend and minor principal stress has eastward direction (e.g., Rao and Kumar 1999; Rao and Kalpna 2005; Kundu and Gahalaut 2012). Kundu and Gahalaut (2012) also suggested that most of the intermediate depth earthquakes in the region are due to reactivation of faults, which already existed within the subducted Indian plate. These events had a reverse fault mechanism with medium dip-angles (~30^o to ~60^o) and strike directions are almost perpendicular to the subduction zone (Figure 2). Hypocenter relocation results from Hurukawa et al. (2012) showed changes of the fault plane dip, which become steeper between 60 and 100 km depth with a dip change from 30^o to 50^o.

Moment tensor and finite-slip inversion

In this section, we invert for the slip distribution to evaluate the fault complexity of the intermediate depth Chauk earthquake. This is done by first applying the moment tensor inversion using teleseismic body-waves (Kikuchi and Kanamori 1982; Kikuchi and Kanamori 2003). The earthquake location reported by the USGS (20.923°N, 94.569°E, origin time: 10:34:54 UTC) was used. It was assumed that the earthquake occurred on a single fault plane. We selected broadband seismogram in the distance range 30^o to 90^o from the Incorporated Research Institutions for Seismology (IRIS) (Figure 3). We used 34 P-waves on the vertical components and 8 SH-waves on the transverse components with a time window of 75 seconds to include P, pP, sP, S, and sS phases. The instrument response was deconvolved to obtain displacement seismograms that were bandpass filtered between 0.01 to 0.2 Hz.

We calculated Green's functions using the Jeffreys-Bullen's model for the source and receivers regions (Jeffreys and Bullen 1940). Attenuation is implemented through t_P^* = 1 s and t_{SH}^* = 4 s. Different source depths were tested from 70 to 110 km, and we found the lowest variance at 90 km depth (Figure 4a). Our results showed that the Chauk 2016 earthquake had a thrust mechanism with either subhorizontal or near vertical fault plane (Strike 1: 323, Dip1: 8, Rake1: 65, Strike2: 168, Dip2: 83, Rake2: 93). While the vertical fault plane is similar to the focal mechanism solutions reported by USGS, and Global CMT, the horizontal fault plane is different From the moment tensor inversion, the seismic moment is M_0=1.55 E+19 Nm, giving a moment magnitude M_W=6.7.

These final results were obtained by excluding stations located around the vertical nodal plane (azimuths around 168±15^o, i.e., CASY, COCO, and 348±15^o, i.e., BFO, GRFO, KBS, KONO) on the lower hemisphere projection plot. The observed and synthetic waveforms of P-waves for these stations do not agree and in some cases, the polarities are flipped. The observed first motions are impulsive rather than emergent (which is expected to occur on stations located close to the nodal plane) and of opposite sign compared to the computed seismograms. These differences can be caused by the complexity of the seismic velocity structure in the source region, resulting in take-off angles different from the angles calculated using 1D model.

To investigate the slip pattern and the source-time function, we carried out a slip inversion for both the sub-horizontal and the near vertical fault planes. The grid size of the fault plane was estimated using the source scaling relation for intraslab earthquake by Strasser et al. (2010). Based on our seismic moment estimate, an area of 30 x 30 km with a grid spacing of 5 km was set for the inversion. One of the significant parameters in the slip inversion is the rupture velocity, and testing a range of values we found that the lowest variance is given by Vr between 1.5 km/s to 2.5 km/s. Since the variances within this range do not differ significantly, we decided to use the median value, 2.0 km/s (Figure 4b). During the inversion, while the strike and dip are fixed, the rake angle is varied up to 45^{o} for each grid cell. The source-time function was constructed using two triangular functions with half duration 2 seconds, and the amplitudes of these functions were determined during the inversion. We could not model the complexity of the observed waveforms with fewer than two triangular functions.

There was little difference in the variance when inverting for slip on either subhorizontal (Figure 5) (variance = 0.34) or subvertical fault plane (Figure S1, available in the electronic supplement to this article, variance = 0.33), which means a preferred solution could not be selected. Both of the models showed that the earthquake had quite a simple slip distribution where the highest slip occurred around the hypocenter, 1.60meters for the horizontal fault plane and 1.61 meters for the vertical fault plane (Figure 4). The source-time function showed that most of the total duration of the moment release is around 12 seconds. From the slip inversion result, the earthquake released a total seismic moment M_0=1.52 E+19 Nm which is equivalent to M_w=6.7.

Source-time function and directivity

Because the actual fault plane could not be identified from either the slip inversion or aftershock distribution, we attempted to resolve this question by studying the directivity effect on apparent source-time functions of stations at teleseismic distances. Source directivity can be seen as change of the duration of the source-time function with station's azimuth (θ) that ruptures unilaterally at a direction φ (e.g., Ben-Menahem and Singh 1981; Cesca et al. 2011)

$$\Delta t = t_r + \frac{L}{V_r} - \frac{L\ \cos(\varphi - \theta)}{v}$$

where L is the rupture length, t_r is the rise time, V_r is the rupture velocity, and v is P-wave or S-wave velocity in the vicinity of the source.

Following Benz and Herrmann (2014), we deconvolved the synthetic waveforms from the vertical components of teleseismic waveforms to obtain station apparent source-time functions (ASTF). We used the *hudson96* code from the Computer Programs in Seismology (CPS) (Herrmann 2013) to calculate synthetic Green's function calculations based on the method explained by Hudson (1969). The ak135 velocity model (Kennett et al. 1995) was used in this process. We performed the deconvolution technique using the *saciterd* code from CPS based on the time-domain iterative approach by Ligorría and Ammon (1999). We used a time window from 10 s before to 40 s after the P-wave onset and a Gaussian filter parameter, alpha, of 0.3. For quality control, predicted traces were created by convolving the ASTFs with synthetic traces and then we calculated their correlations with the observed traces. Only the ASTFs that were able to produce predicted traces with a correlation factor ≥ 75% were used in the directivity analysis (Figure 6a).

We measured the duration of the ASTF for each station by calculating the duration from the point where the amplitude exceeds 15% of the maximum peak until the point where the amplitude drops below 15% of the maximum peak. We then fitted the ASTF vs azimuth with the calculated Δt for different unilateral rupture scenarios in a grid-search procedure. We limited the rupture velocity between 1.5 km/s to 4.5 km/s and changed the fault length from 15 to 30 km. We did not impose any constraint for horizontal fault plane scenario since φ in any direction can still be observed, while on the vertical fault plane scenarios, the directivity effect can only be observed if φ is toward the fault's strike direction or the opposite direction. Therefore, we tested three different rupture scenarios: (1) horizontal fault plane scenario, (2) vertical fault plane scenario with $\varphi=163^o$, (3) vertical fault plane with φ=343 (Figure 6b and 6c). The horizontal fault scenario showed a better fit compared to the other scenarios with L = 24 km, $\varphi = 88^o$ with rupture velocity 2 km/s, and we conclude that the rupture propagated down-dip on the horizontal plane. This rupture propagation showed a similarity with the result from slip inversion using the horizontal fault plane. The average source-time function obtained by stacking the ASTF showed a single main source-time function with ~15 seconds duration.

Stress Drop

We estimated the average stress drop of the 2016 Chauk earthquake using $\Delta\sigma = \mathrm{C}\,\frac{M_O}{A\hat{L}}$, where C is a non-dimensional constant which depends on the fault geometry. M_0 is the seismic moment, A is the fault area, and $\hat{L}$ is either fault length or width. For the dip slip fault, $C = \frac{4(\lambda+\mu)}{\pi(\lambda+2\mu)}$ where μ is rigidity and λ is Lame's coefficient (Aki 1966). Using the velocity and density values from Jeffreys-Bullen's model (Jeffreys and Bullen 1940), we obtained μ = 72,000 MPa and λ = 72,000 MPa.

Using the whole area from the finite-slip model can produce an exaggerated fault size, since the slip at some grids can be close to zero, resulting in underestimated stress drop. Therefore, we used the effective fault dimension definition by Mai and Beroza (2000) to estimate the fault size and adopted the autocorrelation width definition (W^{ACF}) (Bracewell 1986). We first summed the slip along strike direction and along dip direction to obtain the slip function used to obtain the effective length (L_{eff}) and effective width (W_{eff}), respectively. Then we calculated L_{eff} and W_{eff} by normalizing the area under the autocorrelation function with zero lag autocorrelation function:

$$W^{ACF} = \frac{\int_{-\infty}^{\infty}(f * f)dx}{f * f|_{x=0}}$$

We obtained L_{eff} 20 km and W_{eff} 18 km, and the effective area of the fault is 360 km^2. We calculated the stress drop value using the seismic moment from the slip inversion, and obtained a stress drop $\Delta\sigma$ = 20 bars.

Stochastic ground motion simulation

The Chauk 2016 earthquake is the first damaging intermediate depth event recorded on upgraded stations in Myanmar (Thiam et al. 2017) and, therefore, presents an opportunity to investigate ground motion from this type of earthquake in Myanmar. We applied stochastic ground-motion simulation based on a dynamic corner frequency to simulate the ground motion for this event (Motazedian and Atkinson 2005) using the latest version of EXSIM12 (Atkinson et al. 2009). In this simulation, a high corner frequency is applied during the rupture start, and when the rupture grows, the corner frequency becomes lower. The fault is gridded into smaller subfaults, and these contribute to the total ground motion at a seismic station. Two critical parameters in the simulation are the stress drop and the attenuation model (e.g. Bjerrum et al. 2013).

There is currently no appropriate attenuation model for the IBR that could be used in our ground motion modeling. Available models from Northeastern (NE) India are more representative of the stable continental region and would likely underestimate attenuation in Myanmar, e.g. Raghukanth and Somala (2009), where we have propagation through the mantle wedge and Indo-Burmese arc. We therefore used Q values from another subduction zone. The Q-value of $Q(f)=251f^{0.58}$ (Q1) for inslab earthquake in Mexico was adopted (García et al. 2004).

Ground motions were simulated for a total of five stations in Myanmar and Thailand with epicentral distances between ~200 km and ~500 km (Figure 7). The Myanmar stations are MDY, TMU, KTN, and HKA, which are part of the Myanmar National Seismic Network (MM) and CHTO station in Thailand, which is part of the Global Seismic Network (GSN). Thiam et al. (2017) conducted a preliminary site response study using horizontal-to-vertical spectral ratio (H/V) for the new MM network. Site response at MDY shows that H/V ratios are close to 1.While at HKA and KTN, the H/V ratios, on average, are between 1.5 and 2, and H/V ratios at TMU show high peak around 1.5 Hz. However, in this modeling we do not consider site amplification, therefore, we only compare the simulated ground motion with the vertical component records as this component is less affected by site amplification. We used near surface attenuation (κ) ranging from 0.01 to 0.05 by trial and error process. For the geometrical spreading (G) as a function of epicentral distance (R), we use (Singh et al. 1999)

$$G(R) = \begin{cases} R^{-1} & R \le 100\ km \\ (100R)^{-0.5} & R \ge 100\ km \end{cases}$$

We used stress drop of 10, 20, 40 and 80 bars. The residuals (Res) of simulated ground motion for different stress drop scenarios (Ghofrani et al. (2013) modified by Zhang et al. (2016)) were calculated using:

$$Res\ (f) = \ log_{10}(FAS_{obs}) - log_{10}(FAS_{sim})$$

where FAS_{obs} and FAS_{sim} are Fourier Amplitude Spectra for observed and simulated ground motions, respectively. The smoothed average residuals for different stress drop were compared in Figure 8.

We also did the same analysis using an alternative Q model for NE India (Q(f) = $431f^{0.7}$) (Q2) (Raghukanth and Somala 2009), and the result is shown in Figure S2 (available in the electronic supplement to this article). Since the Q model for this region is loosely constraint, we only use the modeling result up to 10 Hz. We compared the average absolute residuals for the different stress drop values. The simulated result for a stress drop of 20 bars has the lowest residual average absolute residual using the Q1 model, while the Q2 model gives lowest residual for a stress drop of 10 bars. However, we prefer the Q1 model for inslab earthquake in Mexico since it is more realistic and overall gave lower residuals. The stress drop of 20 bars using Q1 produced reasonable simulated ground motion (Figure 9). The final parameters used in ground motion modeling are shown in Table 1.

Discussion and Conclusions

The Chauk 2016 earthquake occurred at intermediate depth within the IBR and its understanding gives important insight into the nature of this subduction zone. From the moment tensor inversion, we obtained a thrust mechanism with either subhorizontal or near vertical fault plane. We inverted for the slip model on both of these possible mechanisms. However, from the teleseismic body-wave inversion, we could not select a preferred fault plane as both solutions produced a similar fit with the observed waveforms. We, therefore, performed directivity analysis, by comparing apparent source-time function durations (ASTF) for several stations as function of azimuths. Various scenarios of unilateral rupture propagation for each fault mechanism with different fault length and rupture velocities were tested by fitting them with ASTF for different azimuths. We prefer the subhorizontal fault plane with downdip rupture propagation as it yields better fit with the ASTF.

The Chauk 2016 event occurred within the subducting Indian slab with the P-axis nearly perpendicular to the slab interface. The earthquake had a mechanism with strike near parallel to the subduction and dip angles that are either near vertical or horizontal. Its mechanism is comparable to the Mb=5.4 event in March 1992, which had a normal faulting mechanism, but a similar orientation and stress pattern as the 2016 event.

We plotted the teleseismic double-difference relocation catalog from Pesicek et al. (2010) overlaid with the 2016 event along with its largest aftershock and the 1992 event (Figure 10a). The slab-parallel T-axis direction of the Chauk 2016 event is consistent with the down-dip extension caused by the slab pull force of the subducting Indian slab, which is also shown by several other intermediate depth events in this region. However, the east-west P-axis direction of the 2016 and other events nearby are not consistent with the majority of the intermediate depth earthquakes in this region, which have north-south trends of P-axes (Figure 10b). The predominantly north-south P-axes could be related to horizontal slab compression due to the convergence of India and Eurasia (Steckler et al. 2016).

Astiz et al. (1988) compiled focal mechanism solutions for intermediate depth earthquakes, from various subduction zones, around 33% of them have reverse-fault mechanisms with a strike near parallel to the trench axis and have horizontal compression and down-dip tension axes. Astiz et al. (1988) suggested that these events occurred in the subducted slab of the weekly coupled or uncoupled subduction where the dip of the slab increases, e.g., the Philippines, Kermadec, Solomon Islands, and Hindu-Kush regions.

A recent modeling study of lithospheric bending of the subduction zone suggested that the occurrence of reverse fault intraslab earthquakes with the fault plane parallel to the top of the slab can be explained by the flexural slip scenario (Romeo and Álvarez-Gómez 2018). Their modeling results were consistent with the reverse faulting of the intraslab earthquake in El Salvador and Peru-North Chile subduction zones. The P-axis orientations of these earthquakes are in slab normal directions and the T-axis orientations are slab down-dip.

Fault plane orientation studies of intermediate depth earthquake by observing directivity effect on teleseismic stations has been conducted for several regions by Warren et al. (2007; 2008) and Warren (2014). They found predominantly subhorizontal fault plane directions for intermediate depth events in Tonga-Kermadec, Middle America, and South America subduction zones along with few near vertical fault planes. A back-projection study of intermediate depth earthquakes conducted by Kiser et al. (2011), also showed dominant subhorizontal fault planes in various subduction zones. Kiser et al. (2011) hypothesized that preference of the subhorizontal fault plane reactivation is because of the isobaric condition of this fault compared to the near vertical fault. This isobaric condition allows the fluids, which migrate due to slab dehydration, travel further inside the fault and generates fault slip.

One of the prevailing hypotheses of the generating mechanism of intermediate depth earthquakes is dehydration embrittlement (e.g., Hacker et al. 2003; Jung et al. 2004; Ranero et al. 2005; Frohlich 2006). In this process, the slab temperature increases as it reaches greater depth in the mantle, dehydration occurs and results in the reactivation of pre-existing faults or creation of new faults. Kundu and Gahalaut (2012) suggested that intermediate depth earthquakes beneath IBR occur on previously existing faults that are reactivated as they reach the deeper part of the subduction. Furthermore, they tested the hypothesis by rotating two types of hypothetical faults, i.e., east and west dipping faults which already existed before in the Bay of Bengal and then rotated into nearly vertical and subhorizontal faults, respectively. These faults can be originated from the ridges or as a result of subducting plate bending, as shown by several marine seismic survey in the Bay of Bengal, and Sumatra-Andaman region, e.g. Maurin and Rangin (2009), Singh et al. (2012) and Rangin and Sibuet (2017). The hypothesis of fault reactivation mechanism is proposed by several other studies in different subduction zones, e.g., the Tonga subduction zone (Jiao et al. 2000), the middle America trench (Ranero et al. 2003), and middle America and Chile subduction zones (Ranero et al. 2005). While the generating mechanism for the Chauk earthquake is not obvious, reactivation of a preexisting fault in the subducting continental crust is a feasible explanation.

Furthermore, we calculated the stress drop of the Chauk earthquake. The stress drop is estimated from the obtained slip and fault dimension. To obtain realistic fault dimension, we calculate effective fault dimensions from the slip model because using overall slip area will give larger fault dimension, hence a lower stress drop. The effective area of the fault is 360 km^2, which is smaller than the estimated area of an intraslab earthquake using scaling relation by Strasser et al. (2010). This indicates our estimate of the fault area gives higher stress drop. A stress drop $\Delta\sigma$ = 20 bars is obtained from this analysis. Our estimated stress drop value is lower than the value estimated for other intermediate depth damaging earthquakes e.g. Vrancea 1977 ($\Delta\sigma$ = ~100 bars) (Gusev et al. 2002), which may explain why this earthquake did not create more widespread damage. However, one needs to be aware of the large uncertainty in stress drop estimation.

The ground motions for five stations were simulated using the finite-fault stochastic modeling method. We adopted a quality factor relation for inslab earthquakes in Mexico (Q1) (García et al. 2004) which was already used to model the ground motion of the inslab earthquakes in Mexico, e.g. Rodríguez-Pérez et al. (2015). For comparison, we also conducted ground motion modeling using Q model from Northeast India (Q2) (Raghukanth and Somala 2009).

The effect of different stress drop on ground motion was further explored using a range of 10-80 bars. We obtained the best solution using the 20 bars stress drop in agreement with the estimate obtained from the slip distribution. Different near-surface attenuation values κ were tested between 0.01 to 0.05 based on the site information described in Thiam et al. (2017). The κ value mostly affects the higher frequency portion of the ground motion spectra. The κ values were explored through trial and error process while using site information as a guideline.

Based on our modeling result, for Q1 model, the lowest residual is obtained for the 20 bars stress drop, and for the Q2 model, the 10 bars stress drop gives lowest residual. This simply shows the trade-off between attenuation and stress drop. We assume that Q2 underestimates attenuation along the IBR, and argue that the Q1 modeling is more realistic. With the estimated stress drop of 20 bars and quality factor, we were able to produce reasonable ground motion for stations in Myanmar and Thailand at fault-station distances between ~200 km to ~500 km. However, there are some expected mismatches in parts of the spectra, which can be attributed to lateral heterogeneity of the earth’s attenuation and different site amplifications.

From the detailed analysis of regional and teleseismic seismograms from the Chauk 2016 earthquake, we arrive at to the following main conclusions:

- The Chauk earthquake is an intra-slab intermediate depth events with either horizontal or near vertical fault plane from the teleseismic moment tensor inversion, and the horizontal fault plane is more consistent with the observed directivity effect
- The teleseismic seismograms were explained with a relatively simple source and a single main asperity
- The Chauk earthquake reflects slab pull beneath the Myanmar region as reflected by the down-dip T-axis.
- Stress drop estimation from effective source dimension indicate a fairly regular stress drop of 20 bars

- The regional ground motion was well enough modelled with this stress drop and appropriate assumptions on attenuation

Data and Resources

Teleseismic data of Global Seismic Network (GSN) and Strong Motion Data of Myanmar Seismic Network (MSN) (Department of Meteorology and Hydrology—National Earthquake Data Center 2016) and one GSN station (CHTO) were provided by Incorporated Research Institutions for Seismology (IRIS). The U.S. Geological Survey (USGS) National Earthquake Information Center (NEIC) hypocentre and moment tensor soultions were obtained from https://earthquake.usgs.gov/earthquakes/eventpage/us10006gbf#executive (last accessed December 2017). The International Seismological Centre (ISC) - Engdahl, Hilst and Bulland (EHB) catalog and the Global Centroid Moment Tensor solutions (Dziewonski et al. 1981; Ekström et al. 2012) were downloaded from ISC webpage (http://www.isc.ac.uk/, last accessed April 2018). Some of the figures were created using the Generic Mapping Tools v.4.5.15 (www.soest.hawaii.edu/gmt, last accessed December 2017; Wessel et al. 2013). Teleseismic moment tensor and slip inversion result were obtained using Teleseismic Body-Wave Inversion Program (Kikuchi and Kanamori 2003) (http://wwweic.eri.u-tokyo.ac.jp/ETAL/KIKUCHI/, last accessed December 2017). Apparent source-time function estimation were conducted using Computer Programs in Seismology (Herrmann 2013) and by following a tutorial from http://www.eas.slu.edu/eqc/eqc_cps/TUTORIAL/DECON/index.html (last accessed December 2017). Effective source dimension calculation was performed by utilizing a MATLAB function “effdim” obtained from http://equake-rc.info/CERS-software/effsrcdim/ (last accessed December 2017). Stochastic ground motion modeling code (EXSIM12) were obtained from http://www.seismotoolbox.ca/EXSIM12.html (last accessed December 2017).

Acknowledgements

This research was conducted under "Seismic Monitoring, Myanmar II Project" which is funded by The Royal Norwegian Ministry of Foreign Affairs and The Norwegian Agency for Development Cooperation (Norad). We thank the Editor-in-Chief Zhigang Peng for his suggestions and his effort in handling this manuscript and two anonymous reviewers for their constructive comments. We thank our project partners, Asian Disaster Preparedness Center (ADPC) and Department of Meteorology and Hydrology (DMH), Ministry of Transport and Communication, Myanmar for their support during this project.

References

Aki K (1966) Generation and propagation of G waves from the Niigata earthquake of June 16, 1964. Part 2. Estimation of earthquake moment, released energy, and stress-strain drop from the G wave spectrum.

Altamimi Z, Métivier L, Collilieux X (2012) ITRF2008 plate motion model. J Geophys Res Solid Earth 117:1–14. doi: 10.1029/2011JB008930

Astiz L, Lay T, Kanamori H (1988) Large intermediate-depth earthquakes and the subduction process. Phys Earth Planet Inter 53:80–166. doi: 10.1016/0031-9201(88)90138-0

Atkinson GM, Assatourians K, Boore DM, et al (2009) A guide to differences between stochastic point-source and stochastic finite-fault simulations. Bull Seism Soc Am. doi: 10.1785/0120090058

Aung HH (2017) Myanmar Earthquakes History, 3rd edn. Myanmar Engineering Society, Yangon

Ben-Menahem A, Singh S (1981) Seismic waves and sources. Springer, New York

Benz HM, Herrmann RB (2014) Rapid estimates of the source time function and Mw using empirical green's function deconvolution. Bull Seismol Soc Am 104:1812–1819. doi: 10.1785/0120130325

Bjerrum LW, Sørensen MB, Ottemöller L, Atakan K (2013) Ground motion simulations for İzmir, Turkey: Parameter uncertainty. J Seismol 17:1223–1252. doi: 10.1007/s10950-013-9389-9

Bracewell RN (1986) The Fourier transform and its applications, 2nd edn. McGraw-Hill, New York

Cesca S, Heimann S, Dahm T (2011) Rapid directivity detection by azimuthal amplitude spectra inversion. J Seismol 15:147–164. doi: 10.1007/s10950-010-9217-4

Department of Meteorology and Hydrology—National Earthquake Data Center (2016) Myanmar National Seismic Network. doi: https://doi.org/10.7914/SN/MM

Dziewonski a. M, Chou T-AAT -a. a, Woodhouse JH (1981) Determination of earthquake source parameters from waveform data for studies of global and regional seismicity. J Geophys Res 86:2825. doi: 10.1029/JB086iB04p02825

Ekström G, Nettles M, Dziewoński AM (2012) The global CMT project 2004-2010: Centroid-moment tensors for 13,017 earthquakes. 200–201:1–9. doi: 10.1016/j.pepi.2012.04.002

Engdahl ER, der van Hilst R, Buland R (1998) Global teleseismic earthquake relocation with improved travel times and procedures for depth determination. Bull Seismol Soc Am 88:722–743.

Frohlich C (2006) Deep Earthquakes. Cambridge University Press, Cambridge

García D, Singh SK, Herráiz M, et al (2004) Inslab earthquakes of Central Mexico: Q, source spectra, and stress drop. Bull Seismol Soc Am 94:789–802. doi: 10.1785/0120030125

Ghofrani H, Atkinson GM, Goda K, Assatourians K (2013) Stochastic finite-fault simulations of the 2011 Tohoku, Japan, earthquake. Bull Seismol Soc Am 103:1307–1320. doi: 10.1785/0120120228

Gusev A, Radulian M, Rizescu M, Panza GF (2002) Source scaling of intermediate-depth Vrancea earthquakes. Geophys J Int 151:879–889.

Hacker BR, Peacock SM, Abers GA, Holloway SD (2003) Subduction factory 2. Are intermediate-depth earthquakes in subducting slabs linked to metamorphic dehydration reactions? J Geophys Res Solid Earth. doi: 10.1029/2001JB001129

Herrmann RB (2013) Computer Programs in Seismology: An Evolving Tool for Instruction and Research. Seismol Res Lett 84:1081–1088. doi: 10.1785/0220110096

Hudson JA (1969) A quantitative evaluation of seismic signals at teleseismic distances - II. Body waves and surface waves from an extended source. Geophys J Roy astr Soc 18:353–370.

Hurukawa N, Tun PP, Shibazaki B (2012) Detailed geometry of the subducting Indian Plate beneath the Burma Plate and subcrustal seismicity in the Burma Plate derived from joint hypocenter relocation. Earth, Planets Sp 64:333–343. doi: 10.5047/eps.2011.10.011

Centre IS (2013) On-line Bulletin. http://www.isc.ac.uk. Internatl. Seismol. Cent., Thatcham, United Kingdom. Accessed 1 Apr 2018.

Jeffreys H, Bullen KE (1940) Seismological Tables. British Association Seismological Committee, London.

Jiao W, Silver PG, Fei Y, Prewitt CT (2000) Do intermediate- and deep-focus earthquakes occur on preexisting weak zones? An examination of the Tonga subduction zone. J Geophys Res Solid Earth 105:28125–28138. doi: 10.1029/2000jb900314

Jung H, Green II HW, Dobrzhinetskaya LF (2004) Intermediate-depth earthquake faulting by dehydration embrittlement with negative volume change. Nature 428:545–549.

Kayal JR (2010) Microearthquake seismology and seismotectonics of south asia. Springer, New Delhi

Kennett BLN, Engdahl ER, Buland R (1995) Constraints on seismic velocities in the Earth from traveltimes. Geophys. J. Int. 122:108–124.

Kikuchi M, Kanamori H (1982) Inversion of Complex Body Waves-III. Bull Seismol Soc Am 81:2335–2350.

Kikuchi M, Kanamori H (2003) Note on teleseismic body-wave inversion program.

Kiser E, Ishii M, Langmuir CH, et al (2011) Insights into the mechanism of intermediate-depth earthquakes from source properties as imaged by back projection of multiple seismic phases. J Geophys Res. doi: 10.1029/2010jb007831

Kumar MR, Rao NP, Chalam S V. (1996) A seismotectonic study of the Burma and Andaman arc regions using centroid moment tensor data. Tectonophysics 253:155–165. doi: 10.1016/0040-1951(95)00027-5

Kundu B, Gahalaut VK (2012) Earthquake occurrence processes in the Indo-Burmese wedge and Sagaing fault region. Tectonophysics 524–525:135–146. doi: 10.1016/j.tecto.2011.12.031

Le Dain YA, Tapponnier P, Molnar P (1984) Active faulting and tectonics of Burma and surrounding regions. J Geophys Res 89:453–472. doi: 10.1029/JB089iB01p00453

Li C, van der Hilst RD, Meltzer AS, Engdahl ER (2008) Subduction of the Indian lithosphere beneath the Tibetan Plateau and Burma. Earth Planet Sci Lett 274:157–168. doi: 10.1016/j.epsl.2008.07.016

Ligorría JP, Ammon CJ (1999) Iterative deconvolution and receiver-function estimation. Bull Seismol Soc Am 89:1395–1400.

Mai PM, Beroza GC (2000) Source scaling properties from finite-fault-rupture models. Bull Seismol Soc Am 90:604–615. doi: Doi 10.1785/0119990126

Maurin T, Rangin C (2009) Structure and kinematics of the Indo-Burmese Wedge: Recent and fast growth of the outer wedge. Tectonics 28:n/a-n/a. doi: 10.1029/2008tc002276

Motazedian D, Atkinson GM (2005) Stochastic finite-fault modeling based on a dynamic corner frequency. Bull Seismol Soc Am 95:995–1010. doi: 10.1785/0120030207

Ni JF, Guzman-Speziale M, Bevis M, et al (1989) Accretionary tectonics of Burma and the three-dimensional geometry of the Burma subduction zone. Geology 17:68–71. doi: 10.1130/0091-7613(1989)017<0068:ATOBAT>2.3.CO;2

Paul J, Bürgrmann R, Gaur VK, et al (2001) The motion and active deformation of India. Geophys Res Lett 28:647–650.

Pesicek JD, Thurber CH, Zhang H, et al (2010) Teleseismic double-difference relocation of earthquakes along the Sumatra-Andaman subduction zone using a 3-D model. J Geophys Res 115:B10303. doi: 10.1029/2010JB007443

Raghukanth STG, Somala SN (2009) Modeling of strong-motion data in Northeastern India: Q, stress drop, and site amplification. Bull Seismol Soc Am 99:705–725. doi: 10.1785/0120080025

Ranero CR, Phipps Morgan J, McIntosh K, Reichert C (2003) Bending-related faulting and mantle serpentinization at the Middle America trench. Nature 425:367–373.

Ranero CR, Villaseñor A, Morgan JM, Weinrebe W (2005) Relationship between bend-faulting at trenches and intermediate-depth seismicity. Geochemistry, Geophys

Geosystems 6:n/a-n/a. doi: 10.1029/2005gc000997

Rangin C, Sibuet J-C (2017) Structure of the northern Bay of Bengal offshore Bangladesh: Evidences from new multi-channel seismic data. Mar Pet Geol 84:64–75. doi: 10.1016/j.marpetgeo.2017.03.020

Rao NP, Kalpna (2005) Deformation of the subducted Indian lithospheric slab in the Burmese arc. Geophys Res Lett 32:1–5. doi: 10.1029/2004GL022034

Rao NP, Kumar MR (1999) Evidences for cessation of Indian plate subduction in the Burmese arc region. Geophys Res Lett 26:3149–3152. doi: 10.1029/1999GL005396

Rodríguez-Pérez Q, Ottemöller L, Raeesi M (2015) Source study of three moderate size recent earthquakes in the Guerrero seismic gap. J Seismol 19:753–780. doi: 10.1007/s10950-015-9493-0

Romeo I, Álvarez-Gómez JA (2018) Lithospheric folding by flexural slip in subduction zones as source for reverse fault intraslab earthquakes. Sci Rep 8:1–9. doi: 10.1038/s41598-018-19682-7

Satyabala SP (1998) Subduction in the Indo-Burma Region: Is it still active? Geophys Res Lett 25:3189–3192.

Singh SC, Chauhan APS, Calvert AJ, et al (2012) Seismic evidence of bending and unbending of subducting oceanic crust and the presence of mantle megathrust in the 2004 Great Sumatra earthquake rupture zone. Earth Planet Sci Lett 321:166–176. doi: https://doi.org/10.1016/j.epsl.2012.01.012

Singh SK, Ordaz M, Dattatrayam RS, Gupta HK (1999) A spectral analysis of the 21 May 1997, Jabalpur, India, earthquake (Mw = 5.8) and estimation of ground motion from future earthquakes in the Indian shield region. Bull Seismol Soc Am 89:1620–1630.

Steckler MS, Mondal DR, Akhter SH, et al (2016) Locked and loading megathrust linked to active subduction beneath the Indo-Burman Ranges. Nat Geosci 9:615–618. doi: 10.1038/ngeo2760

Strasser FO, Arango MC, Bommer JJ (2010) Scaling of the Source Dimensions of Interface and Intraslab Subduction-zone Earthquakes with Moment Magnitude. Seismol Res Lett 81:941–950. doi: 10.1785/gssrl.81.6.941

Thiam HN, Min Htwe YM, Kyaw TL, et al (2017) A Report on Upgraded Seismic Monitoring Stations in Myanmar: Station Performance and Site Response. Seismol Res Lett 88:1–9. doi: 10.1785/0220160168

Tun ST, Wang Y, Khaing SN, et al (2014) Surface ruptures of the Mw 6.8 march 2011 tarlay earthquake, Eastern Myanmar. Bull Seismol Soc Am 104:2915–2932. doi: 10.1785/0120130321

Wang Y, Sieh K, Tun ST, et al (2014) Active tectonic and earthquake Myanmar region. J Geophys Res Solid Earth 119:3767–3822. doi: 10.1002/2013JB010762.Received

Warren LM (2014) Dominant fault plane orientations of intermediate-depth earthquakes beneath South America. J Geophys Res Solid Earth 119:5762–5785. doi: 10.1002/2013jb010856

Warren LM, Hughes AN, Silver PG (2007) Earthquake mechanics and deformation in the Tonga-Kermadec subduction zone from fault plane orientations of intermediate- and deep-focus earthquakes. J Geophys Res. doi: 10.1029/2006jb004677

Warren LM, Langstaff MA, Silver PG (2008) Fault plane orientations of intermediate-depth earthquakes in the Middle America Trench. J Geophys Res. doi: 10.1029/2007jb005028

Wessel P, Smith WHF, Scharroo R, et al (2013) Generic mapping tools: improved version released. EOS Trans AGU. doi: 10.1002/2013eo450001

Weston J, Engdahl ER, Harris J, et al (2018) ISC-EHB: Reconstruction of a robust earthquake dataset. Geophys J Int ggy155-ggy155.

Zaw SH, Ornthammarath T, Poovarodom N (2017) Seismic reconnaissance and observed damage after the Mw 6.8, 24 August 2016 Chauk (Central Myanmar) earthquake. J Earthq Eng 2469:13632469.2017.1323050-13632469.2017.1323050. doi: 10.1080/13632469.2017.1323050

Zhang L, Chen G, Wu Y, Jiang H (2016) Stochastic ground-motion simulations for the 2016 Kumamoto, Japan, earthquake. Earth, Planets Sp 68:184. doi: 10.1186/s40623-016-0565-3

Figure Captions:

Figure 1. (a) Tectonic map of Myanmar. Active fault locations (Wang et al., 2014) are shown as black lines. The black arrow is the velocity of Indian plate relative to Eurasian plate based on the ITRF 2008 model (Altamimi et al. 2012). The star gives the location of the Mw 6.8 2016 event. Black rectangles are cities mentioned in the text (BGN: Bagan, MDY; Mandalay). (b) Seismicity map of Myanmar taken from ISC-EHB catalog (Engdahl et al. 1998; Weston et al. 2018)

Figure 2. Intermediate depth earthquakes in Myanmar with M > 5.4. The contours of the top of the Wadati-Benioff zone are shown as dashed blue lines (Hurukawa et al., 2012). Focal mechanisms, P- and T-axes are taken from Global CMT catalog. The star is the epicenter of the Chauk 2016 earthquake.

Figure 3. Station distribution for moment tensor and slip inversion. The red star gives the epicenter location. Blue inverted triangles are seismic stations labeled with station name.

Figure 4. (a) Depth vs variance for telesiesmic moment tensor inversion. Slip distribution for two fault plane solutions: subhorizontal fault plane (b), and vertical fault plane (c). For both subfigures: top: source-time function, middle: focal mechanism, bottom: slip distribution.

Figure 5. Observed (thick lines) and synthetic waveforms (thin lines) obtained in the slip inversion for horizontal fault plane. The P-wave is recorded on the vertical component while SH-wave is on the transverse component. The numbers below the phases label are the station azimuths.

Figure 6. (a) Apparent source-time functions at teleseismic stations used in this study. (b) Apparent STF duration vs azimuth along with calculated STF duration for three unilateral rupture scenarios. (c) Calculated STF duration for the horizontal rupture scenario with different rupture velocity Vr.

Figure 7. Location of five stations in Myanmar and Thailand that are used for stochastic ground motion modeling.

Figure 8. Average smoothed residuals comparison for 10, 20, 40, and 80 bars stress drop models.

Figure 9. Smoothed Fourier amplitude spectra of simulated and observed ground motion for five stations. Each station is labelled with epicentral distance (R) and κ value.

Figure 10. (a) Cross-section showing the depth distribution of earthquakes in the relocated EHB catalog [*Pesicek et al.*, 2010], along with mechanisms of the Mw 6.7 2016 event and M 5.4 1992 event (GCMT) and the location of the cross-section. The stars are the location of the 2016 event along with its aftershock and the 1992 event (each events are labelled with magnitude and year) (b) Cross-section illustration of the mechanism of the 2016 Myanmar earthquake along with the seismicity from Figure 10.a.

Table Caption

Table 1. Parameters used for stochastic finite fault modeling.

Figure 1

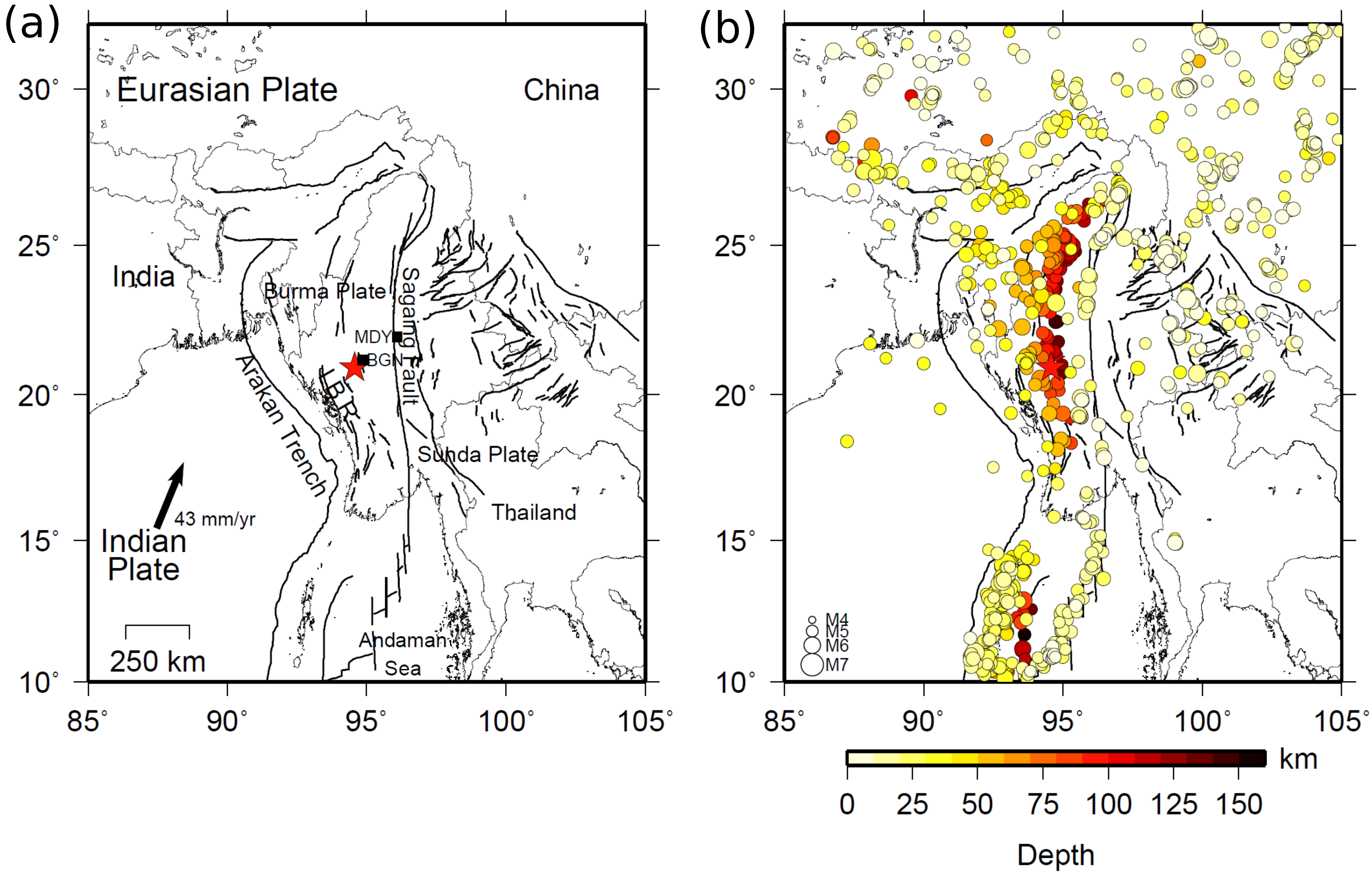

(a)
Eurasian Plate
China
India
Burma Plate
Sagaing Fault
MDY
BGN
IBR
Arakan Trench
Sunda Plate
Thailand
43 mm/yr
Indian Plate
250 km
Andaman Sea
30°
25°
20°
15°
10°
85°
90°
95°
100°
105°
(b)
M4
M5
M6
M7
0
25
50
75
100
125
150
km
Depth

Figure 2

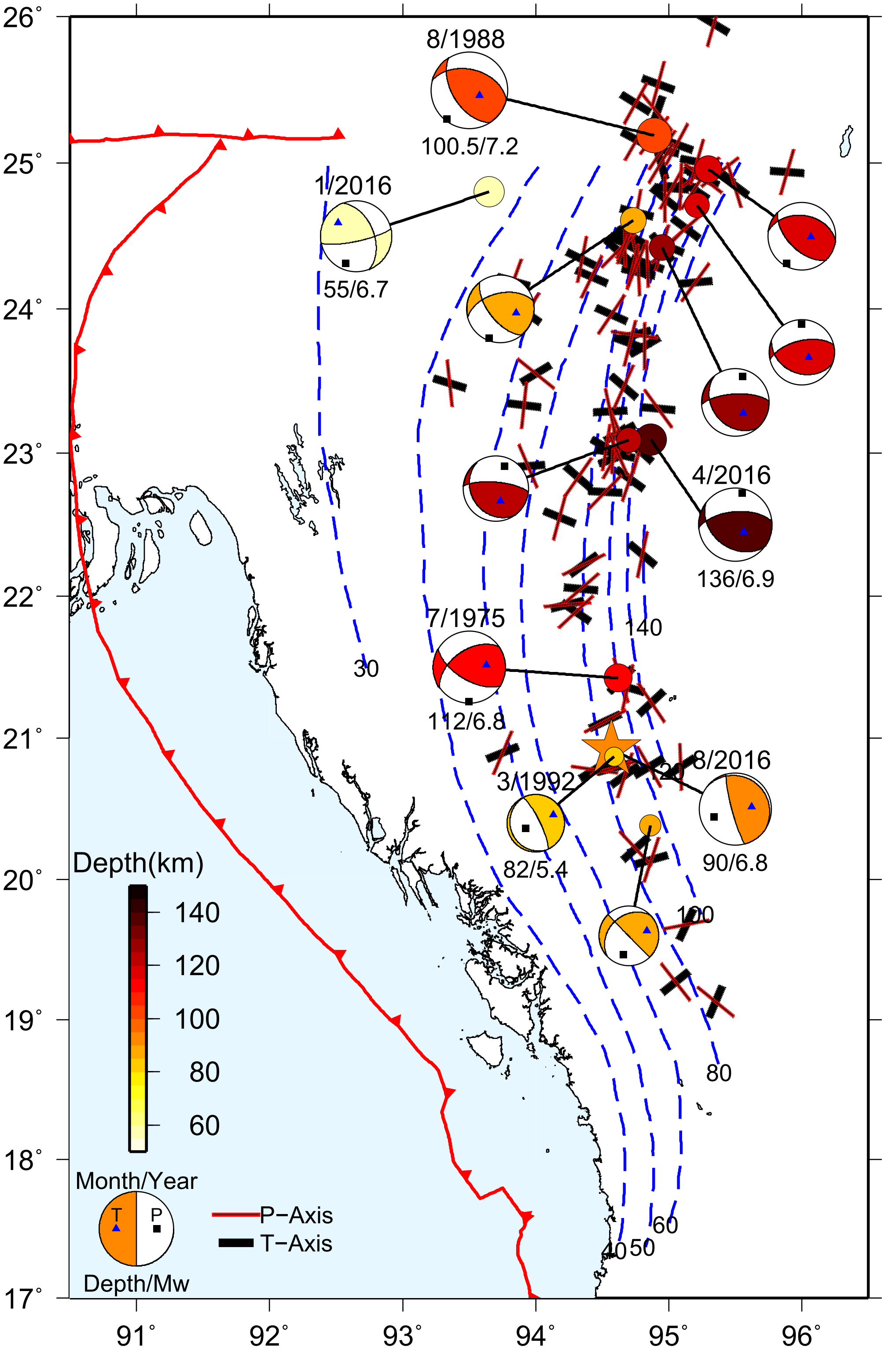

26°
25°
24°
23°
22°
21°
20°
19°
18°
17°
91°
92°
93°
94°
95°
96°
8/1988
100.5/7.2
1/2016
55/6.7
4/2016
136/6.9
7/1975
112/6.8
3/1992
82/5.4
8/2016
90/6.8
30
140
120
100
80
60
50
40
Depth(km)
140
120
100
80
60
Month/Year
T
P
Depth/Mw
P−Axis
T−Axis

Figure 3

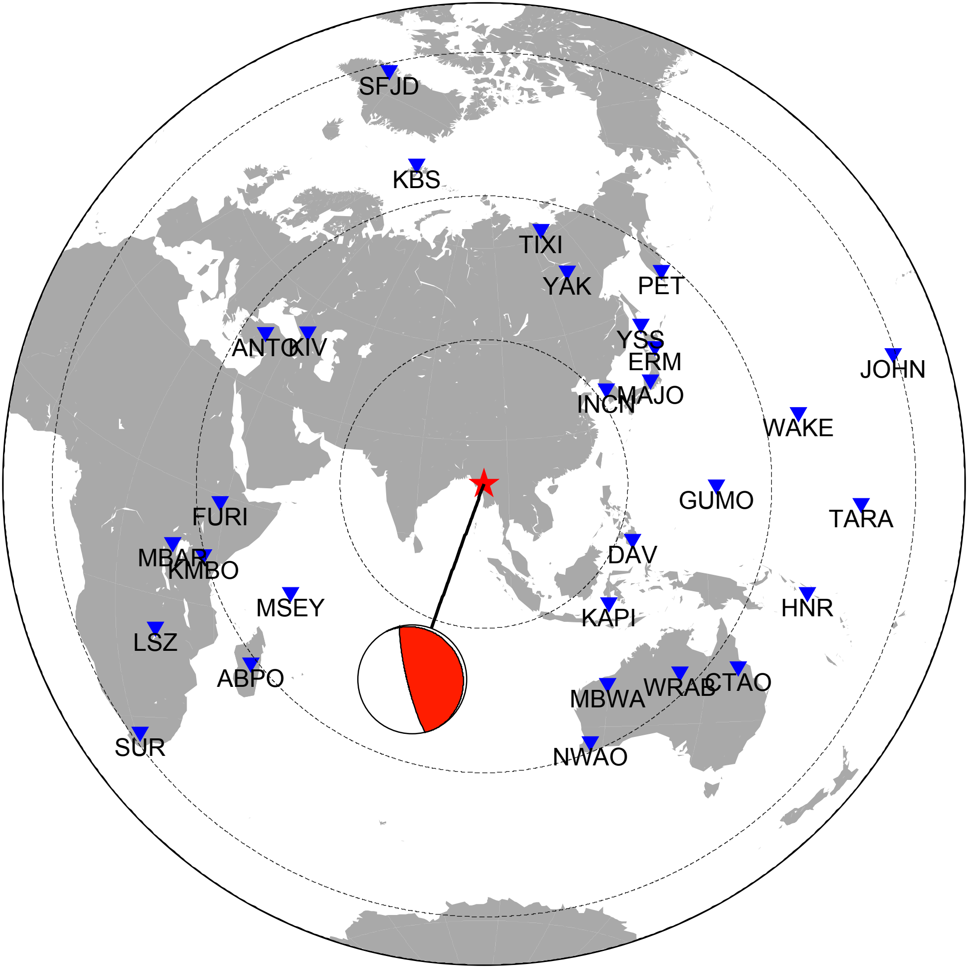

SFJD
KBS
TIXI
YAK
PET
YSS
ERM
JOHN
MAJO
INCN
ANTO
KIV
WAKE
GUMO
TARA
FURI
DAV
MBAR
KMBO
MSEY
HNR
KAPI
LSZ
ABPO
MBWA
WRAB
CTAO
SUR
NWAO

Figure 4

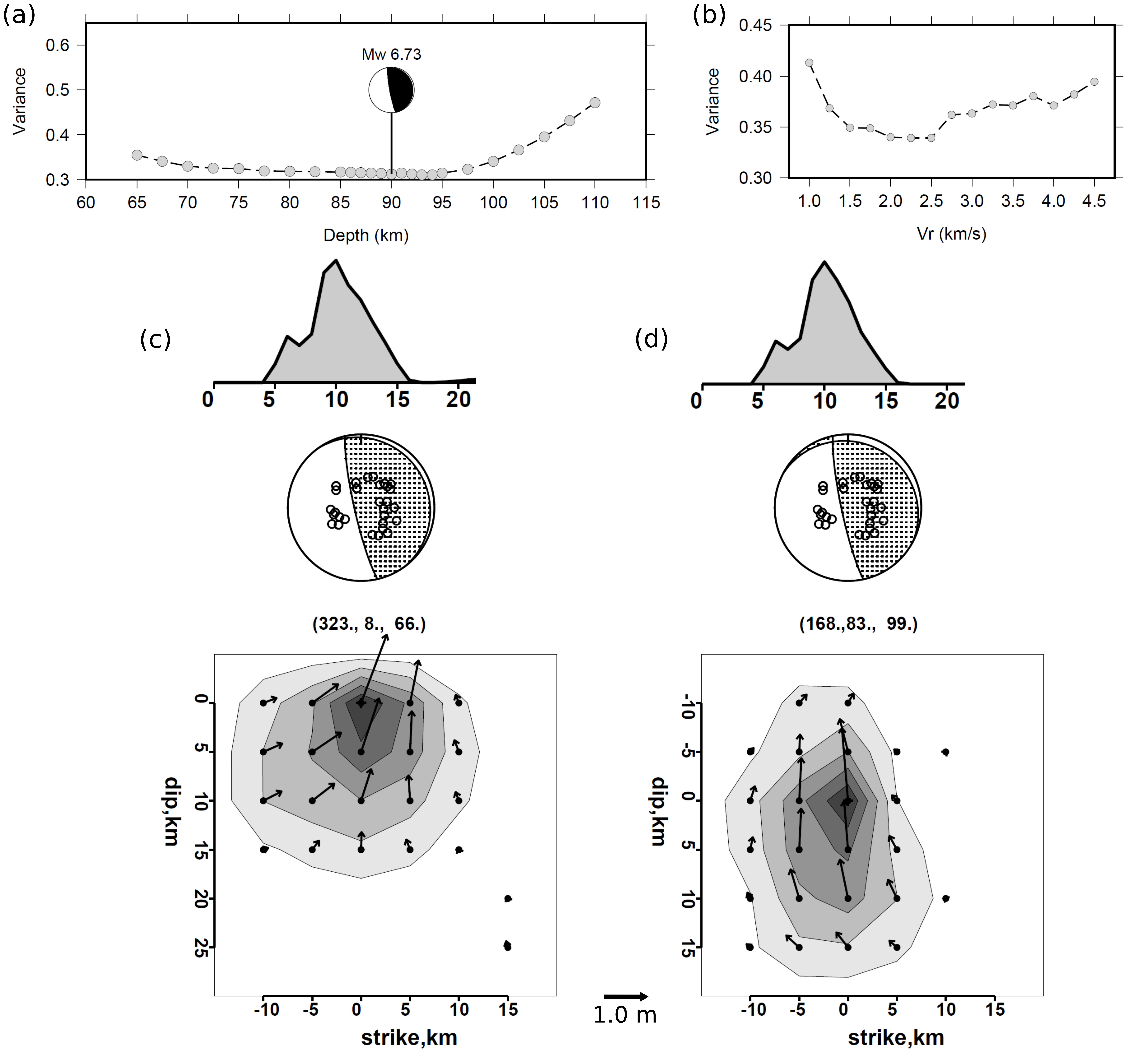

(a)
Mw 6.73
Variance
Depth (km)
(b)
Variance
Vr (km/s)
(c)
(d)
(323., 8., 66.)
(168.,83., 99.)
dip,km
strike,km
1.0 m

Figure 5


0
20
40
60
II.ABPO.00 SH 232.6
II.ABPO.00 P 232.6
II.ERM.00 P 51.1
II.KAPI.10 P 133.7
II.KIV.00 SH 310.8
II.KIV.00 P 310.8
II.MBAR.10 P 259.5
II.MSEY.10 P 240.8
II.SUR.10 P 234.2
II.WRAB.00 P 133.8
IU.ANTO.00 P 304.8
IU.CTAO.00 SH 125.7
IU.CTAO.00 P 125.7
IU.DAV.00 P 110.3
IU.FURI.10 P 266.3
IU.GUMO.10 P 90.2
IU.HNR.00 SH 108.5
IU.HNR.00 P 108.5
IU.INCN.00 P 52.0
IU.JOHN.00 P 72.3
IU.KBS.00 SH 348.1
IU.KBS.00 P 348.1
IU.KMBO.00 P 255.9
IU.LSZ.00 P 246.5
IU.MAJO.10 SH 57.8
IU.MAJO.10 P 57.8
IU.MBWA.10 P 148.2
IU.NWAO.00 P 157.6
IU.PET.00 P 39.7
IU.SFJD.00 SH 347.1
IU.SFJD.00 P 347.1
IU.TARA.10 P 92.9
IU.TIXI.00 P 12.6
IU.WAKE.10 P 77.2
IU.YAK.00 P 21.4
IU.YSS.00 SH 44.3
IU.YSS.00 P 44.3

Figure 6

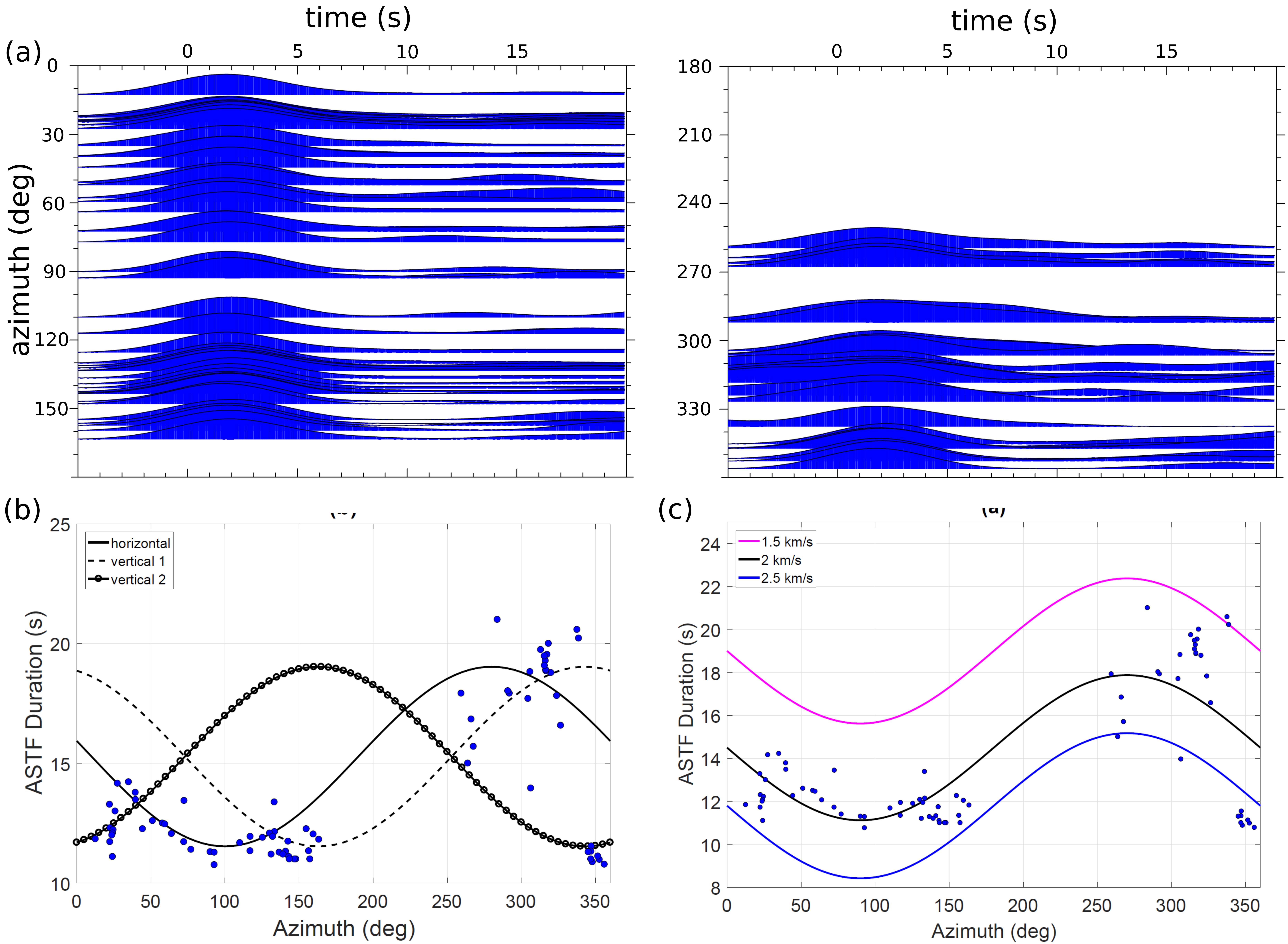

(a)
time (s)
0
5
10
15
azimuth (deg)
0
30
60
90
120
150
time (s)
180
210
240
270
300
330
(b)
ASTF Duration (s)
25
20
15
10
horizontal
vertical 1
vertical 2
0
50
100
150
200
250
300
350
Azimuth (deg)
(c)
1.5 km/s
2 km/s
2.5 km/s
24
22
20
18
16
14
12
10
8
ASTF Duration (s)
Azimuth (deg)

Figure 7

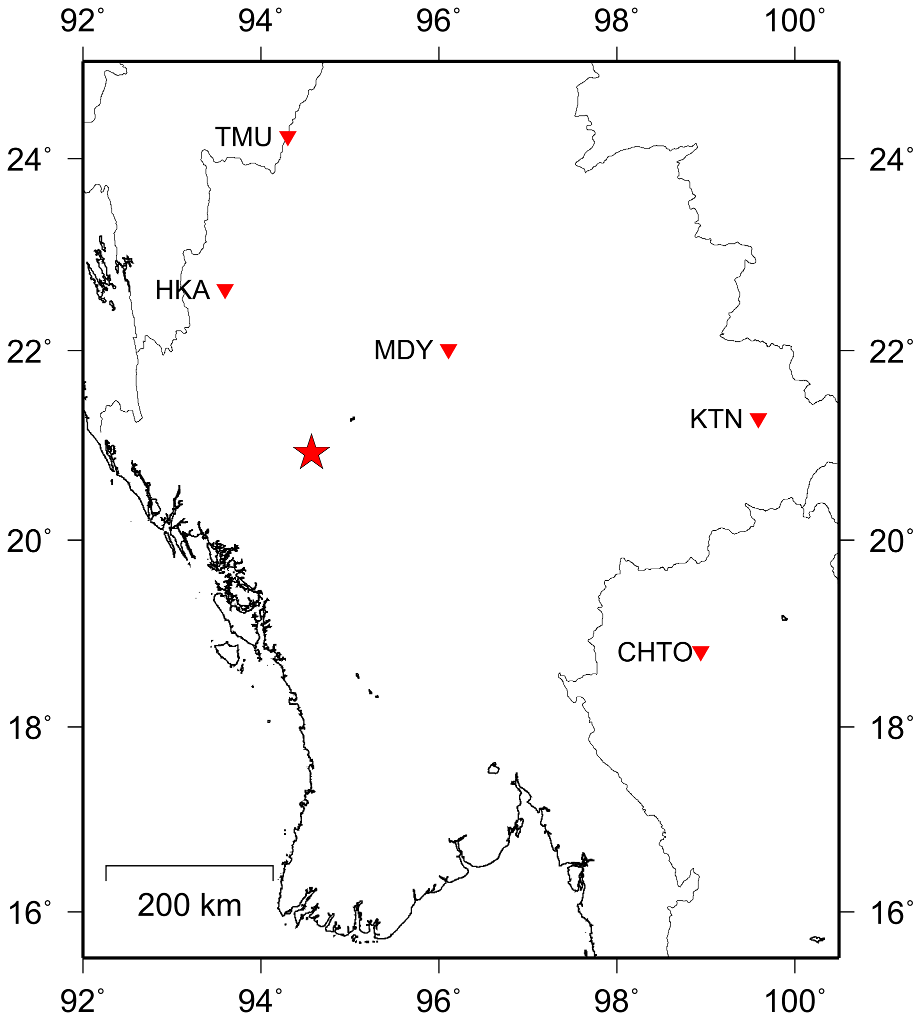

Figure 8

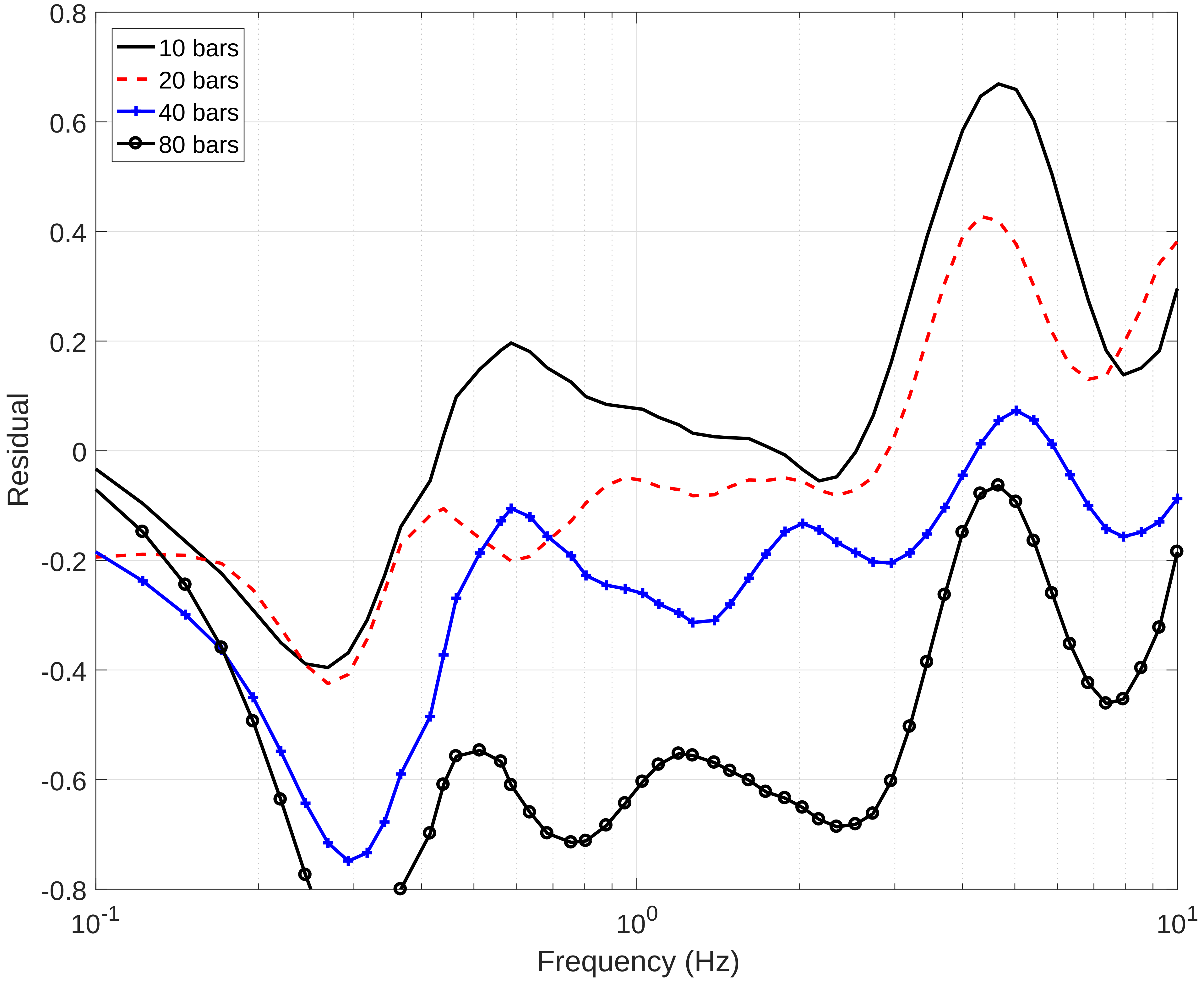

10 bars
20 bars
40 bars
80 bars
0.8
0.6
0.4
0.2
0
-0.2
-0.4
-0.6
-0.8
Residual
10^{-1}
10^{0}
10^{1}
Frequency (Hz)

Figure 9


(a)
simulated
observed
MDY, R = 200.7 km, kappa = 0.01
FAS (m/s)
Frequency (Hz)
Simulated
Observed (Z)
Amplitude(m/s²)
Time (s)
(b)
simulated
observed
HKA, R = 215.8 km, kappa = 0.04
FAS (m/s)
Frequency (Hz)
Simulated
Observed (Z)
Amplitude(m/s²)
Time (s)
(c)
simulated
observed
TMU, R = 368.7 km, kappa = 0.01
FAS (m/s)
Frequency (Hz)
Simulated
Observed (Z)
Amplitude(m/s²)
Time (s)
(d)
simulated
observed
CHTO, R = 514.1 km, kappa = 0.03
FAS (m/s)
Frequency (Hz)
Simulated
Observed (Z)
Amplitude(m/s²)
Time (s)
(e)
simulated
observed
KTN, R = 522.4 km, kappa = 0.01
FAS (m/s)
Frequency (Hz)
Simulated
Observed (Z)
Amplitude(m/s²)
Time (s)

Figure 10

(a)
Depth (km)
0
−50
−100
−150
−200
0
100
200
300
400
500
Distance (km)
A
B
M5.4, 1992
M6.8, 2016
M4.5, 2016
24
22
20
18
90
92
94
96
98
M6.8, 2016
M5.4, 1992
A
B
200
175
150
125
100
75
50
25
0
Depth (km)
(b)
Burma
Plate
Indian
Plate
P
T

Table 1. Parameters used for stochastic finite fault ground motion modeling.

Parameter	**Value**
Vs	4.28 km/s
Rupture velocity	0.5 Vs
Q(f)	$251f^{0.58}$
κ	0.02 – 0.04
$\Delta\sigma$	10, 20, 40, 80 bars

Electronics Supplement to

Source study of the 24 August 2016 M_w=6.8 Chauk earthquake, Myanmar

By Hasbi A Shiddiqi, Pa Pa Tun, Tun Lin Kyaw, and Lars Ottemöller

This electronic supplement contains the figure that shows the observed and synthetics waveforms obtained from the slip inversion for the vertical fault plane scenario, and the residuals comparison of stochastic ground motion modeling result using the Q model from Northeast India (Raghukanth and Somala 2009).

S1. Observed (thick lines) and synthetic waveforms (thin lines) obtained in the slip inversion for fault plane. The P-wave is recorded on the vertical component while SH-wave is on the transverse component. The numbers below the phases label are the station azimuths.

S2. Average smoothed residuals comparison for 10, 20, 40, and 80 bars models using Q model from Northeast India.

Reference:

Raghukanth STGG, Somala SN (2009) Modeling of strong-motion data in Northeastern India: Q, stress drop, and site amplification. Bull Seismol Soc Am 99:705–725. doi: 10.1785/0120080025


0
20
40
60
II.ABPO.00 SH 232.6
II.ABPO.00 P 232.6
II.ERM.00 P 51.1
II.KAPI.10 P 133.7
II.KIV.00 SH 310.8
II.KIV.00 P 310.8
II.MBAR.10 P 259.5
II.MSEY.10 P 240.8
II.SUR.10 P 234.2
II.WRAB.00 P 133.8
IU.ANTO.00 P 304.8
IU.CTAO.00 SH 125.7
IU.CTAO.00 P 125.7
IU.DAV.00 P 110.3
IU.FURI.10 P 266.3
IU.GUMO.10 P 90.2
IU.HNR.00 SH 108.5
IU.HNR.00 P 108.5
IU.INCN.00 P 52.0
IU.JOHN.00 P 72.3
IU.KBS.00 SH 348.1
IU.KBS.00 P 348.1
IU.KMBO.00 P 255.9
IU.LSZ.00 P 246.5
IU.MAJO.10 SH 57.8
IU.MAJO.10 P 57.8
IU.MBWA.10 P 148.2
IU.NWAO.00 P 157.6
IU.PET.00 P 39.7
IU.SFJD.00 SH 347.1
IU.SFJD.00 P 347.1
IU.TARA.10 P 92.9
IU.TIXI.00 P 12.6
IU.WAKE.10 P 77.2
IU.YAK.00 P 21.4
IU.YSS.00 SH 44.3
IU.YSS.00 P 44.3

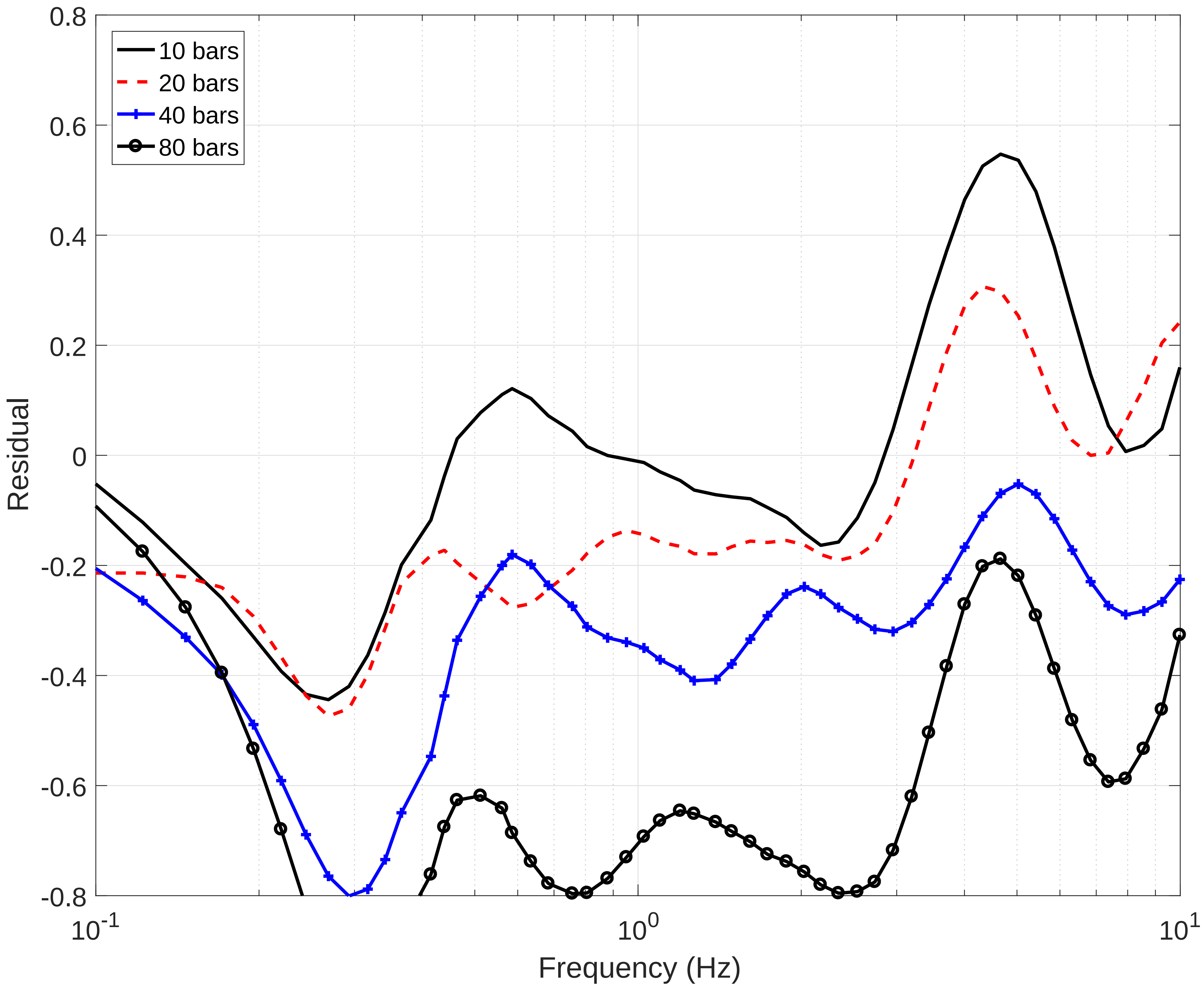

10 bars
20 bars
40 bars
80 bars
0.8
0.6
0.4
0.2
0
-0.2
-0.4
-0.6
-0.8
Residual
10^{-1}
10^{0}
10^{1}
Frequency (Hz)